

# Schwarzschild Black Holes Immersed in Born-Infeld Magnetic Fields and Their Observational Signatures

Yiqian Chen<sup>b,\*</sup>, Guangzhou Guo<sup>c,†</sup>, Benrong Mu<sup>a,‡</sup> and Peng Wang<sup>d§</sup>

<sup>a</sup>*Center for Joint Quantum Studies, College of Medical Technology,*

*Chengdu University of Traditional Chinese Medicine, Chengdu, 611137, PR China*

<sup>b</sup>*School of Fundamental Physics and Mathematical Sciences, Hangzhou Institute for Advanced Study,  
University of Chinese Academy of Sciences, Hangzhou, 310024, China*

<sup>c</sup>*Department of Physics, Southern University of Science and Technology, Shenzhen, 518055, China and*

<sup>d</sup>*College of Physics, Sichuan University, Chengdu, 610064, China*

We investigate the influence of Born-Infeld (BI) nonlinear electrodynamics on magnetic field configurations, photon orbits, and black hole shadows for Schwarzschild black holes immersed in magnetic fields. Assuming that the BI magnetic fields are asymptotically uniform and aligned with the polar axis, we solve the nonlinear magnetic field equations numerically using pseudospectral methods. Our analysis shows that nonlinear electromagnetic effects become prominent near the event horizon, particularly in the polar regions, where the magnetic field strength is significantly enhanced. This enhancement leads to closed photon orbits on the meridional plane becoming prolate, with noticeable stretching along the polar axis. Simulations of black hole images reveal that, at high observer inclinations, the shadow, which is circular in the Maxwell limit, becomes increasingly elongated along the polar direction as the nonlinear effects increase.

---

\* [chenyiqian@ucas.ac.cn](mailto:chenyiqian@ucas.ac.cn)

† [guogz@sustech.edu.cn](mailto:guogz@sustech.edu.cn)

‡ [benrongmu@cdutcm.edu.cn](mailto:benrongmu@cdutcm.edu.cn)

§ [pengw@scu.edu.cn](mailto:pengw@scu.edu.cn)

## CONTENTS

<a href="#">I. Introduction</a>	2
<a href="#">II. Born-Infeld Magnetic Field</a>	4
<a href="#">III. Observational Signatures</a>	7
<a href="#">A. Light Ray</a>	7
<a href="#">B. Celestial Sphere</a>	10
<a href="#">C. Accretion Disk</a>	12
<a href="#">IV. Conclusion</a>	14
<a href="#">Acknowledgments</a>	15
<a href="#">References</a>	15

## I. INTRODUCTION

The recent release of the first horizon-scale image of the supermassive black hole M87\* by the Event Horizon Telescope (EHT) collaboration represents a major milestone in black hole astrophysics [1–6]. This achievement was followed by the publication of the image of Sgr A\*, the supermassive black hole at the center of the Milky Way [7–12], marking the beginning of a new era in testing general relativity in the strong-field regime. Black hole images are typically characterized by a central dark region—referred to as the “shadow”—surrounded by a bright emission ring associated with closed photon orbits. These features are interpreted as direct consequences of strong gravitational lensing, which significantly deflects light near black holes [13–16].

The finite resolution of black hole images leaves room for alternative models that can reproduce the observed features within current observational uncertainties. Utilizing EHT data, it is possible to place constraints on the parameters of models that deviate from the Kerr geometry, thereby enhancing our understanding of the black hole environment [17–22]. In recent years, the black hole shadow and related optical phenomena have been extensively studied across a variety of theoretical frameworks, including hairy black holes [23–30], string inspired black holes [31–34], fuzzball [35], exotic ultra-compact objects [36–43], naked singularities [44–48], and modified gravity theories [49–58].

To further refine the image of M87\*, the EHT collaboration employed GRMHD simulations to reconstruct its polarized structure [59]. The results from these simulations support the existence of a magnetically arrested disk surrounding the black hole [60–62]. Moreover, strong magnetic fields have been detected near Sgr A\*, the supermassive black hole at the center of the Milky Way [63]. Motivated by such observations, the influence of magnetic fields on black hole images has become an active area of study [64–66]. In the extreme environments near black holes—where magnetic fields can reach immense strengths—the assumption that the electromagnetic sector is accurately described by Maxwell’s linear electrodynamics may no longer hold. This motivates the investigation of alternative nonlinear electrodynamics theories. Indeed, the impact of nonlinear electrodynamics on black hole shadows has been explored in various works [67–71]. In particular, black holes immersed in external magnetic fields provide a natural setting to probe nonlinear electromagnetic effects, especially in relation to observational signatures detectable by current and future astronomical facilities [72–74].

Among various nonlinear electrodynamics theories, Born-Infeld (BI) electrodynamics—originally inspired by string theory—stands out for its role in describing the low-energy dynamics of D-branes [75–78]. One of the key features of BI electrodynamics is the introduction of a maximal electric field, which regularizes the electrostatic self-energy of point charges [79]. Recent integrations of BI electrodynamics into gravity frameworks have generated significant theoretical interest [80–90]. Specifically, for a Schwarzschild black hole immersed in an asymptotically uniform magnetic field, perturbative solutions for the BI magnetic field and the resulting black hole shadow have been obtained by considering only the lowest-order corrections due to BI nonlinearities [74, 91]. However, the full non-perturbative solution for the BI magnetic field in the Schwarzschild background remains unknown. This work addresses this gap by numerically solving the BI field equations with boundary conditions ensuring asymptotic uniformity, employing pseudospectral methods for accuracy and efficiency.

The remainder of this paper is organized as follows. In Sec. II, we numerically compute the BI magnetic field configuration in the Schwarzschild black hole background and analyze its behavior with varying nonlinearity parameter. In Sec. III, we investigate the resulting closed photon orbits and simulate black hole images for different values of the nonlinearity parameter and observer inclination. Finally, we summarize our main findings in Sec. IV. We set  $G = c = 4\pi\epsilon_0 = 1$  throughout the paper.

## II. BORN-INFELD MAGNETIC FIELD

In this section, we consider an asymptotically uniform BI magnetic field in the Schwarzschild black hole background, aligned along the  $z$ -axis. The BI magnetic field is governed by the Lagrangian density [79],

$$\mathcal{L}(F) = -\frac{4}{a} \left( 1 - \sqrt{1 + \frac{aF}{2}} \right), \quad (1)$$

where  $a$  is the nonlinearity parameter,  $F = F^{\mu\nu}F_{\mu\nu}$ , and  $F_{\mu\nu} = \partial_\mu A_\nu - \partial_\nu A_\mu$  is the electromagnetic field strength tensor. In the limit  $a \rightarrow 0$ , the BI theory reduces to Maxwell electrodynamics. Neglecting the backreaction of the BI field, the background spacetime is described by the Schwarzschild metric,

$$ds^2 = -f(r)dt^2 + \frac{1}{f(r)}dr^2 + r^2(d\theta^2 + \sin^2\theta d\varphi^2), \quad (2)$$

where the metric function is  $f(r) = 1 - 2M/r$ , with  $M$  denoting the mass of the black hole.

By varying the Lagrangian in Eq. (1) with respect to the electromagnetic field  $A_\mu$ , one obtains the equation of motion,

$$\partial_\mu \left( \frac{\sqrt{-g}F^{\mu\nu}}{\sqrt{1+aF/2}} \right) = 0. \quad (3)$$

For an asymptotically uniform magnetic field, we adopt the ansatz,

$$A = u(r, \theta)d\varphi, \quad (4)$$

where  $A_t = 0$ , as we consider a purely magnetic configuration without electric charge. In the Maxwell limit  $a = 0$ , the equation of motion (3) admits the analytical solution [92],

$$u(r, \theta) = \frac{1}{2}B_0r^2\sin^2\theta. \quad (5)$$

To numerically solve the partial differential equation in Eq. (3), appropriate boundary conditions for the ansatz  $u(r, \theta)$  must be specified. Since the BI magnetic field is assumed to become uniform at spatial infinity, the solution should be symmetric with respect to reflection across the equatorial plane and approach the asymptotic linear solution given in Eq. (5) in the far-field regime [91]. Accordingly, the function  $u(r, \theta)$  should satisfy the following boundary conditions,

$$\partial_\theta u(r, \theta)|_{\theta=\pi/2} = 0, \quad \lim_{r \rightarrow \infty} u(r, \theta)/r^2 = B_0 \sin^2(\theta)/2. \quad (6)$$

Additionally, a power series expansion of  $u(r, \theta)$  near  $\theta = 0$  and  $r = 0$  yields the conditions,

$$u(r, \theta)|_{\theta=0} = 0, \quad \partial_r u(r, \theta)|_{r=0} = 0. \quad (7)$$

In this work, we employ pseudospectral methods to numerically solve the nonlinear partial differential equation given in Eq. (3), subject to the boundary conditions specified in Eqs. (6) and (7). Pseudospectral methods are a well-established approach for solving partial differential equations [93]. The function  $u(r, \theta)$  is approximated by a finite sum of basis functions as

$$u(r, \theta) = \sum_{i=0}^{N_x-1} \sum_{j=0}^{N_\theta-1} \alpha_{ij} T_i(\tilde{r}) \cos(2j\theta), \quad (8)$$

where  $N_x$  and  $N_\theta$  are the spectral resolutions in the radial and angular directions, respectively,  $T_i(\tilde{r})$  denotes the Chebyshev polynomials, and  $\alpha_{ij}$  are the spectral coefficients.

To compactify the radial domain, we introduce a coordinate transformation,

$$\tilde{r} = \frac{\sqrt{r^2 - r_H^2} - r_H}{\sqrt{r^2 - r_H^2} + r_H}, \quad (9)$$

which maps the event horizon  $r_H = 2M$  to  $\tilde{r} = -1$  and spatial infinity to  $\tilde{r} = 1$ . We choose a spectral resolution of  $(N_x, N_\theta) = (22, 22)$  to balance accuracy and computational efficiency. The spectral expansion in Eq. (8) is substituted into the equation of motion, and the resulting expressions are evaluated at Gauss-Chebyshev collocation points. This procedure transforms the partial differential equation into a system of algebraic equations for the coefficients  $\alpha_{ij}$ , which we solve using a standard Newton-Raphson iteration. At each iteration, the resulting linear system is solved using the built-in `LinearSolve` function in Mathematica.

Once  $u(r, \theta)$  (and consequently  $F_{\mu\nu}$ ) is determined, the magnetic field  $B$  measured by an observer with four-velocity  $U^\mu$  is given by

$$B^i \equiv -\frac{1}{2} \epsilon^{i\nu\rho\sigma} U_\nu F_{\rho\sigma}, \quad (10)$$

where  $\epsilon^{\mu\nu\rho\sigma} \equiv -\tilde{\epsilon}^{\mu\nu\rho\sigma}/\sqrt{-g}$  is the Levi-Civita tensor,  $\tilde{\epsilon}^{\mu\nu\rho\sigma}$  denotes the permutation symbol, and the index  $i$  denotes spatial components. Specifically, we consider a static observer defined by the following orthonormal tetrad:

$$e^{(t)} = \sqrt{1 - \frac{2M}{r}} dt, \quad e^{(r)} = \frac{1}{\sqrt{1 - \frac{2M}{r}}} dr, \quad e^{(\theta)} = r d\theta, \quad e^{(\varphi)} = r \sin \theta d\varphi. \quad (11)$$

In this tetrad frame, the components of the magnetic field are expressed as

$$B^{(r)} = \frac{1}{r^2 \sin \theta} \partial_\theta u(r, \theta), \quad B^{(\theta)} = -\frac{\sqrt{1 - 2M/r}}{r \sin \theta} \partial_r u(r, \theta), \quad B^{(\varphi)} = 0, \quad (12)$$

indicating that  $B^{(\theta)} = 0$  at the event horizon. This implies that the magnetic field lines are perpendicular to the horizon surface. As a consistency check, we compare our numerical results

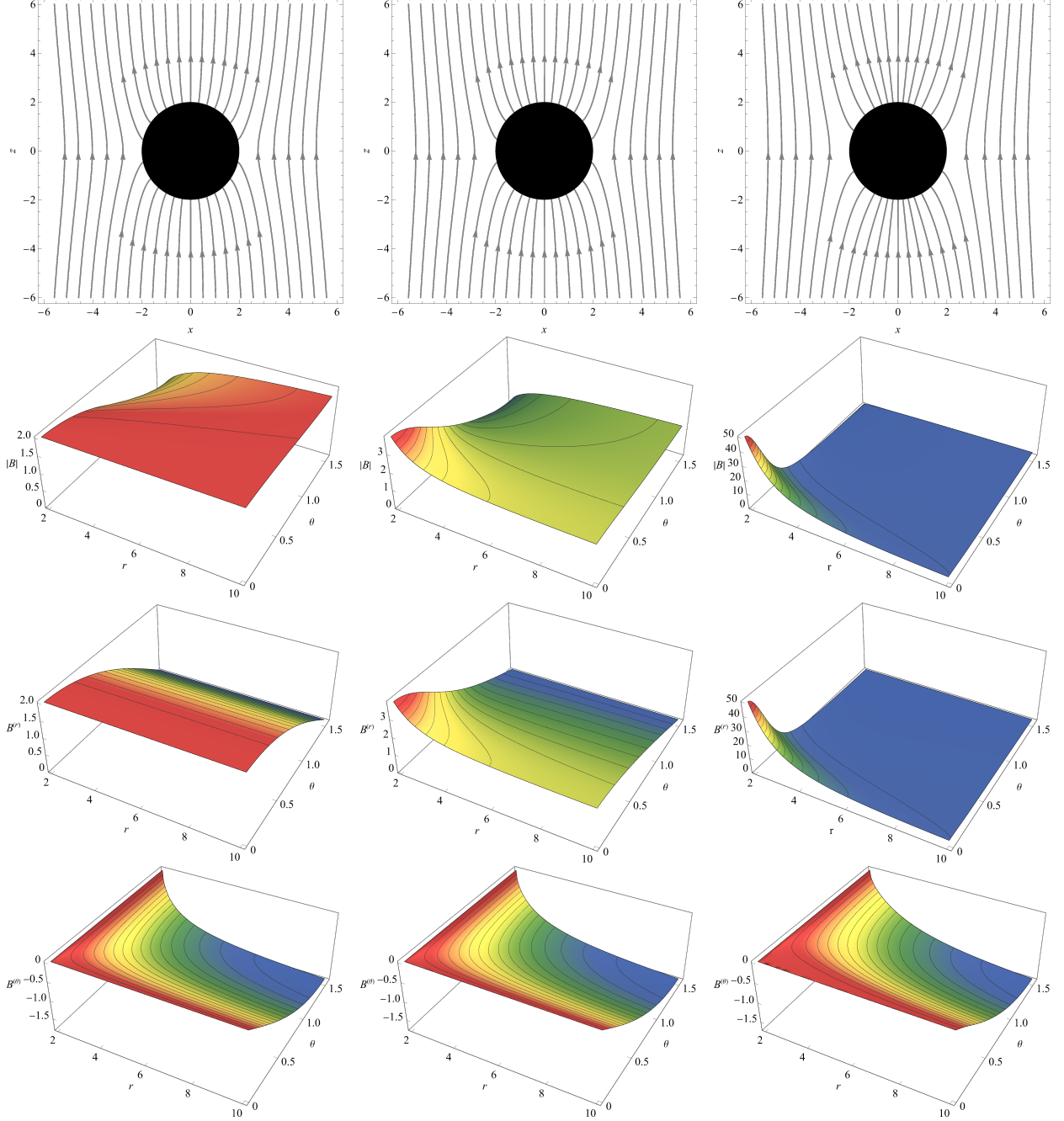


FIG. 1. Magnetic field configurations around a Schwarzschild black hole for different values of the nonlinearity parameter:  $a = 0$  (**Left**),  $a = 0.5$  (**Middle**), and  $a = 2$  (**Right**), with  $M = 1$  and  $B_0 = 2$ . **Top Row:** Magnetic field lines in the  $\varphi = 0$  plane (spanned by  $x$  and  $z$ ). The overall structure is similar across different  $a$ , but line density increases near the polar axis close to the horizon as  $a$  increases. **Second Row:** Magnitude of the magnetic field  $|B|$ , which shows enhancement near the polar region for nonzero  $a$ . **Third Row:** Radial tetrad component  $B^{(r)}$ . Nonlinear effects primarily influence  $B^{(r)}$ . **Bottom Row:** Polar tetrad component  $B^{(\theta)}$ , which remains similar across  $a$ .

for small  $a$  with the perturbative solutions for the BI magnetic field presented in [74, 91], and find good agreement.

Fig. 1 illustrates magnetic field configurations around a Schwarzschild black hole for three representative values of the nonlinearity parameter:  $a = 0$  (left column),  $a = 0.5$  (middle column), and  $a = 2$  (right column). For simplicity, we set  $M = 1$  and  $B_0 = 2$ . The top row shows magnetic field lines in the  $\varphi = 0$  plane, spanned by the Cartesian coordinates  $x$  and  $z$ . While the overall structure remains similar across different  $a$  values, the field line density near the polar axis close to the event horizon increases noticeably with  $a$ . The second row presents the magnitude of the magnetic field  $|B|$ , which generally decreases with increasing polar angle  $\theta$  near the black hole. In the Maxwell limit,  $|B|$  remains nearly constant near the polar axis, whereas in the BI cases, it exhibits a pronounced enhancement toward the horizon. This enhancement intensifies with increasing  $a$ , consistent with the increased field line density. The third and bottom rows show the radial tetrad component  $B^{(r)}$  and polar tetrad component  $B^{(\theta)}$ , respectively. As expected,  $B^{(\theta)}$  vanishes precisely on the event horizon for all values of  $a$ , in agreement with the field lines shown in the top row and the analytic result in Eq. (12). Near the equatorial plane,  $B^{(\theta)}$  dominates the field magnitude, while  $B^{(r)}$  becomes the leading component away from the plane. Moreover, the distribution of  $B^{(\theta)}$  remains largely unchanged across different  $a$ , indicating that nonlinear electromagnetic effects predominantly influence the radial component  $B^{(r)}$ .

### III. OBSERVATIONAL SIGNATURES

In this section, we first analyze null geodesics in the effective geometry induced by BI magnetic fields. We then investigate optical appearances of Schwarzschild black holes immersed in BI magnetic fields, illuminated by either a luminous celestial sphere or a geometrically and optically thin accretion disk. Throughout this section, we set  $M = 1$  and  $B_0 = 2$ .

#### A. Light Ray

Nonlinear electrodynamics theories introduce self-interactions of the electromagnetic field, which in turn modify the propagation of photons. Consequently, photons no longer follow null geodesics with respect to the background metric  $g_{\mu\nu}$ . To describe the trajectories of light rays in the presence of a nonlinear magnetic field, an effective geometry must be employed. As shown in [74, 94], the

effective metric  $G_{\mu\nu}$  for BI electrodynamics is given by

$$G^{\mu\nu} = \partial_F \mathcal{L}(F) g^{\mu\nu} - 4\partial_F^2 \mathcal{L}(F) F_\alpha^\mu F^{\alpha\nu}, \quad (13)$$

with inverse  $G^{\lambda\mu}$  satisfying  $G^{\lambda\mu} G_{\mu\nu} = \delta_\nu^\lambda$ .

Accordingly, the motion of a photon is governed by the geodesic equation,

$$\frac{d^2 x^\mu}{d\lambda^2} + \Gamma_{\rho\sigma}^\mu \frac{dx^\rho}{d\lambda} \frac{dx^\sigma}{d\lambda} = 0, \quad (14)$$

where  $\lambda$  is an affine parameter, and the Christoffel symbols  $\Gamma_{\rho\sigma}^\mu$  are computed with respect to the effective metric  $G_{\mu\nu}$ . The photon trajectory also satisfies the Hamiltonian constraint  $\mathcal{H} = G_{\mu\nu} p^\mu p^\nu / 2 = 0$ , where  $p^\mu = dx^\mu / d\lambda$ . Given that the spacetime admits two Killing vectors,  $K^\mu = (1, 0, 0, 0)$  and  $R^\mu = (0, 0, 0, 1)$ , the following conserved quantities arise,

$$\begin{aligned} E &= -K_\mu p^\mu = -q_t, \\ L &= R_\mu p^\mu = q_\varphi, \end{aligned} \quad (15)$$

where the dual momentum vector  $q_\mu \equiv G_{\mu\nu} p^\nu$ . The quantities  $E$  and  $L$  correspond to the photon's conserved energy and angular momentum, respectively.

When light rays are confined to the equatorial plane with  $\theta = \pi/2$ , the radial component of the geodesic equation takes the form

$$-\frac{G_{tt}(r, \pi/2) G_{rr}(r, \pi/2)}{L^2} \left( \frac{dr}{d\lambda} \right)^2 = \frac{E^2}{L^2} - V_{\text{eff}}(r), \quad (16)$$

where the effective potential is defined as  $V_{\text{eff}}(r) = -G_{tt}(r, \pi/2) / G_{\varphi\varphi}(r, \pi/2)$ . Unstable circular photon orbits on the equatorial plane at radius  $r = r_c$  are determined by the conditions

$$V_{\text{eff}}(r_c) = E^2 / L^2, \quad V'_{\text{eff}}(r_c) = 0, \quad V''_{\text{eff}}(r_c) < 0, \quad (17)$$

where primes denote derivatives with respect to the radial coordinate  $r$ . Due to axisymmetry, light rays may also propagate within the meridional plane defined by  $\varphi = 0$ . On this plane, the magnetic field lines are symmetric about the  $z$ -axis. As a result, closed photon orbits in the meridional plane are expected to exhibit reflection symmetry about the  $z$ -axis, implying  $p^r = 0$  at  $\theta = 0$ . To identify such closed orbits, we numerically integrate Eq. (14), initiating the light ray at  $(r, \theta) = (r_c, 0)$ , and search for the critical value of  $r_c$  that results in a closed trajectory.

Fig. 2 displays closed orbits of photons for different values of the BI nonlinearity parameter  $a$ . The left panel shows these orbits on the equatorial plane, while the right panel illustrates them on the meridional plane. In both panels, the dashed black circle represents the event horizon. For

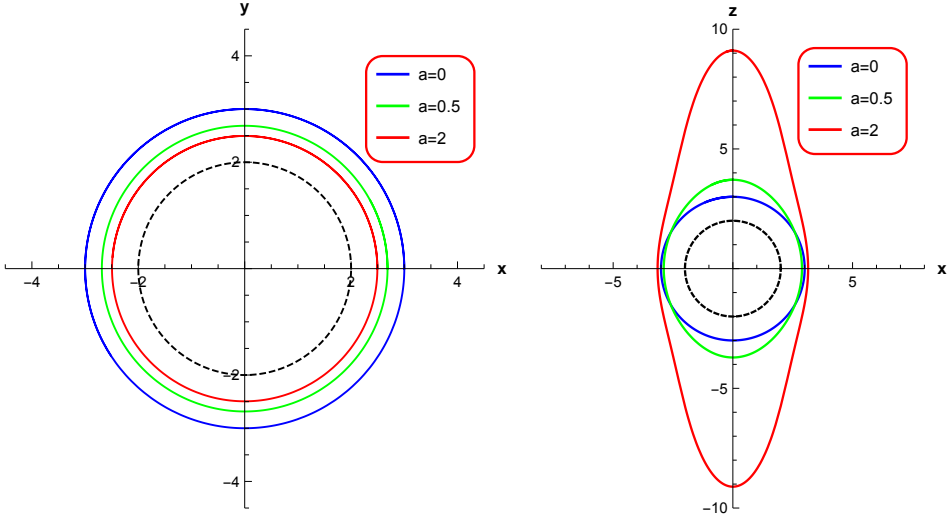


FIG. 2. Closed photon orbits on the equatorial plane with  $\theta = \pi/2$  (**Left**) and the meridional plane with  $\varphi = 0$  (**Right**) for various values of the parameter  $a$ . The dashed black circle indicates the event horizon. For  $a = 0$  (Maxwell case), closed orbits are circular. With increasing  $a$ , closed orbits shrink on the equatorial plane. On the meridional plane, closed orbits become prolate, stretching along the  $z$ -axis. The closed orbit for  $a = 0.5$  is slightly compressed along the  $x$ -axis relative to  $a = 0$ , while for  $a = 2$ , it is slightly stretched.

$a = 0$ , which corresponds to the linear Maxwell theory, the closed orbits are circular in both planes. As the parameter  $a$  increases, indicating a stronger nonlinear electromagnetic effect, the closed orbits deform. On the equatorial plane, the orbits shrink inwards, becoming smaller circles. On the meridional plane, the deviation from circularity becomes more pronounced, stretching along the  $z$ -axis while remaining symmetric with respect to the  $z$ -axis. In particular, the orbit corresponding to  $a = 2$  develops a noticeable elongation along the  $z$ -axis, highlighting the significant impact of nonlinear electromagnetic effects on photon trajectories in strong-field regions.

To image black holes, we employ a numerical backward ray-tracing method to trace light rays from observers to emitting sources. Initial conditions for Eq. (14) are set by considering the photon 4-momentum measured by a static observer located at  $x_o^\mu = (t_o, r_o, \theta_o, \varphi_o)$ <sup>1</sup>,

$$p^{(t)} = p^t \sqrt{-g_{tt}(x_o)}, \quad p^{(r)} = p^r \sqrt{g_{rr}(x_o)}, \quad p^{(\theta)} = p^\theta \sqrt{g_{\theta\theta}(x_o)}, \quad p^{(\varphi)} = p^\varphi \sqrt{g_{\varphi\varphi}(x_o)}. \quad (18)$$

The observation angles  $(\alpha, \beta)$  are defined via the photon's local momentum components as in [37],

$$\sin \alpha = \frac{p^{(\theta)}}{|\vec{P}|}, \quad \tan \beta = \frac{p^{(\varphi)}}{p^{(r)}}, \quad (19)$$

<sup>1</sup> Note that a different observer, one static with respect to the effective geometry, was considered in [74]. This choice leads to shadows stretched along the equatorial plane, rather than the polar direction.

where  $|\vec{P}| = \sqrt{p^{(r)2} + p^{(\theta)2} + p^{(\varphi)2}}$ . The photon momentum  $p^\mu(x_o)$  serves as the initial data for tracing geodesics backward to the emission region. By imposing the Hamiltonian constrain  $\mathcal{H} = 0$  and normalizing the local spatial momentum to  $|\vec{P}| = 1$ , the initial momentum is uniquely determined by the observation angles  $\alpha$  and  $\beta$ . The observer's image plane coordinates  $(x, y)$  are defined as

$$x \equiv -r_o\beta, \quad y \equiv r_o\alpha, \quad (20)$$

where the zero observation angles  $(0, 0)$  correspond to the direction pointing toward the black hole center.

## B. Celestial Sphere

We now investigate images of a Schwarzschild black hole immersed in BI magnetic fields and illuminated by a luminous celestial sphere. The celestial sphere is assumed to have a radius of  $r_{\text{CS}} = 100$  and is concentric with the black hole. A static observer is located at  $r_o = 50$ , with a field of view spanning  $\pi/3$ . To construct the images, we numerically integrate  $2000 \times 2000$  null geodesics from the observer's location, continuing each ray until it either intersects the celestial sphere or falls into the event horizon. The celestial sphere is divided into four quadrants, each assigned a distinct color (see Fig. 2 in [95]). Additionally, we overlay a grid of black lines representing constant longitude and latitude, with adjacent lines separated by  $\pi/18$ .

Fig. 3 displays the images of the celestial sphere as observed for a black hole immersed in BI magnetic fields, highlighting the effects of various the nonlinearity parameter  $a$  and the observer inclination angle  $\theta_o$ . The columns correspond to  $a = 0$  (left),  $a = 0.5$  (middle), and  $a = 2$  (right), while the top and bottom rows depict inclination angles of  $\theta_o = 90^\circ$  and  $\theta_o = 30^\circ$ , respectively. A uniform color grid on the celestial sphere is distorted by gravitational lensing near the black hole, forming a central black hole shadow (gray region). A sequence of higher-order images of the celestial sphere emerges near the shadow edge, gradually accumulating due to light deflection. As the BI nonlinearity increases (i.e., with larger  $a$ ), the initially circular black hole shadow becomes increasingly elongated along the vertical direction. This elongation is associated with the stretching of closed photon orbits along the  $z$ -axis on the meridional plane, as discussed in Fig. 2. The deformation becomes less pronounced at lower inclination angles, such as  $\theta_o = 30^\circ$ , where the observer views the black hole from a more polar direction. Additionally, while the black hole shadow exhibits reflection symmetry about the equatorial plane when  $\theta_o = 90^\circ$ , this symmetry is

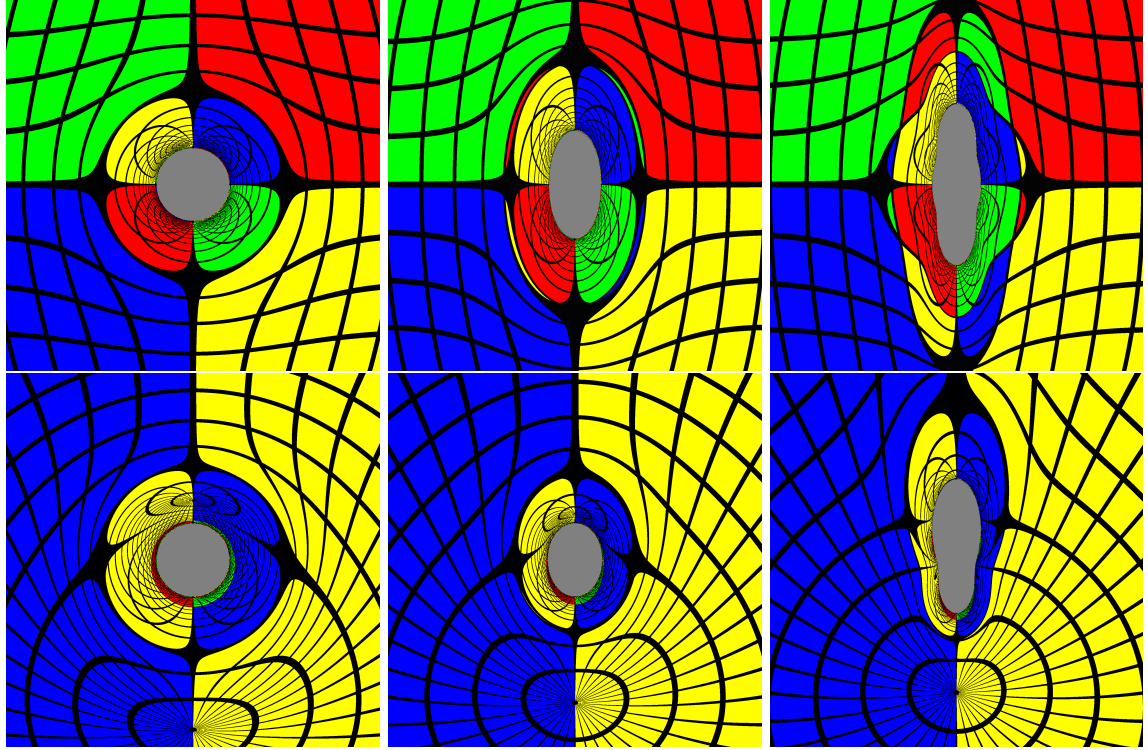


FIG. 3. Celestial sphere images for a Schwarzschild black hole immersed in BI magnetic fields with various nonlinearity parameters:  $a = 0$  (**Left**),  $a = 0.5$  (**Middle**), and  $a = 2$  (**Right**). The top and bottom rows correspond to observer inclination angles  $\theta_o = 90^\circ$  and  $\theta_o = 30^\circ$ , respectively. The celestial sphere is divided into four colored quadrants and overlaid with a grid of black lines. Gravitational lensing distorts the pattern, producing a central black hole shadow (gray region) surrounded by higher-order images of the celestial sphere. As  $a$  increases, the shadow becomes increasingly elongated along the vertical direction due to nonlinear effects. This elongation diminishes with lower inclination angles, and the shadow's equatorial symmetry is broken when  $\theta_o \neq 90^\circ$ .

broken for  $\theta_o = 30^\circ$ .

As  $a$  increases, the color pattern in the celestial sphere images becomes more intricate, particularly for  $\theta_o = 90^\circ$ . For example, in the first quadrant of the image with  $a = 0$  and  $\theta_o = 90^\circ$ , only two colors—red and blue—are visible. This pattern arises because light rays are confined to a single plane when  $a = 0$ . In contrast, when  $a > 0$ , four colors appear in the same quadrant, indicating that some light rays are no longer restricted to a single plane due to the nonlinear effects of the BI magnetic field.

### C. Accretion Disk

We now examine images of a Schwarzschild black hole immersed in BI magnetic fields and illuminated by a geometrically and optically thin accretion disk located in the equatorial plane. The observed intensity at specific image coordinates  $(\alpha, \beta)$  is given by

$$I_o(\alpha, \beta) = \sum_{m=1} g^4(r_m(\alpha, \beta)) j_e(r_m(\alpha, \beta)), \quad (21)$$

where  $r_m(\alpha, \beta)$  denotes the radial position of the  $m$ -th intersection between the light ray (traced backward from  $(\alpha, \beta)$ ) and the accretion disk. The function  $g(r_m)$  represents the redshift factor between the observed photon frequency and the emitted frequency at  $r = r_m$  [96]. Following [97], light rays with  $m = 1$ ,  $m = 2$ , and  $m \geq 3$  constitute the direct emission, lensing ring, and photon ring, respectively. For simplicity, we adopt the emission profile

$$j_e(r) = \frac{e^{-[\text{arcsinh}(2r)-3/2]^2/2}}{\sqrt{r^2 + 1/4}}. \quad (22)$$

The accretion disk is assumed to be rotating: matter outside the Innermost Stable Circular Orbit (ISCO) follows timelike circular geodesics in the equatorial plane, while matter inside the ISCO plunges into the black hole, retaining the same specific energy and angular momentum as at the ISCO. For a photon with four-momentum  $p^\mu$ , the redshift factor is given by  $g = p_\mu u_o^\mu / p_\nu u_e^\nu$ , where  $u_o^\mu$  and  $u_e^\nu$  are four-velocities of the observer and the emitter, respectively. Throughout this paper, the observer is assumed to be static, with  $u_o^\mu = (1/\sqrt{f(r_o)}, 0, 0, 0)$ . For a Schwarzschild black hole, the ISCO radius is  $r_{\text{ISCO}} = 6$ . Following [96], the four-velocity of the emitter outside the ISCO is

$$u_e^t = \frac{1}{\sqrt{1 - 3/r}}, \quad u_e^\varphi = \frac{1}{r^{3/2} \sqrt{1 - 3/r}}, \quad (23)$$

while inside the ISCO, it is given by

$$u_e^t = \frac{2\sqrt{2}}{3} \frac{1}{1 - 2/r}, \quad u_e^r = -\frac{1}{3} \left( \frac{6}{r} - 1 \right)^{3/2}, \quad u_e^\varphi = \frac{6}{\sqrt{3}r^2}. \quad (24)$$

The top row of Fig. 4 shows the images of the rotating accretion disk as viewed by a face-on observer at  $\theta_o = 0^\circ$ , for nonlinearity parameters  $a = 0$ ,  $0.5$ , and  $2$ . For this viewing angle, the images exhibit circular symmetry. Each image reveals a disk-like direct emission region surrounding a central shadow, overlaid by a thin, intensely bright lensing ring. Notably, the sizes of both the shadow and the lensing ring vary non-monotonically with  $a$ : they are largest for  $a = 2$ , intermediate for  $a = 0$ , and smallest for  $a = 0.5$ . This non-monotonic behavior is closely associated with the

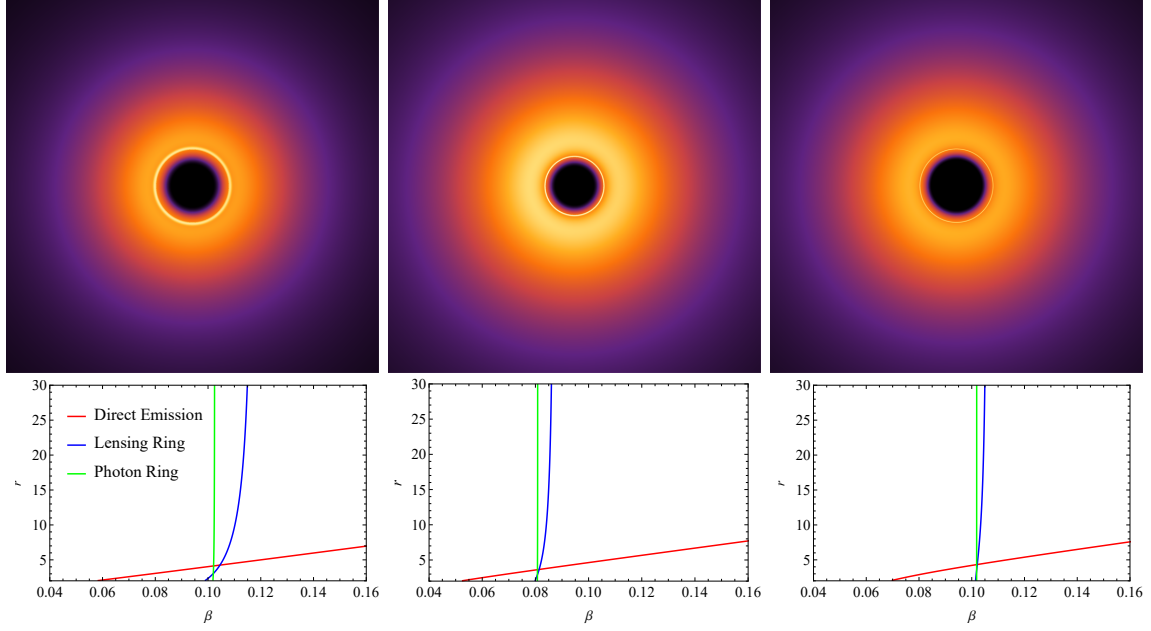


FIG. 4. **Top Row:** Images of a rotating accretion disk around a Schwarzschild black hole immersed in BI magnetic fields, viewed by a face-on observer at  $\theta_o = 0^\circ$ , for nonlinearity parameters  $a = 0$  (**Left**),  $0.5$  (**Middle**), and  $2$  (**Right**). Each image displays a circularly symmetric disk-like emission region, a central shadow, and a bright lensing ring. The sizes of the shadow and lensing ring vary non-monotonically with  $a$ . **Bottom Row:** The corresponding transfer function  $r_m(0, \beta)$  for the direct emission ( $m = 1$ ), lensing ring ( $m = 2$ ), and photon ring ( $m \geq 3$ ). The lensing ring becomes progressively narrower with increasing  $a$ .

compression and stretching of bound photon orbits along the  $x$ -axis on the meridional plane for  $a = 0.5$  and  $a = 2$ , respectively. The bottom row of Fig. 4 plots  $r_m(0, \beta)$  as a function of  $\beta$ , referred to as the transfer function, for the direct emission ( $m = 1$ ), lensing ring ( $m = 2$ ), and photon ring ( $m \geq 3$ ). Both rows demonstrate that the lensing ring becomes significantly narrower as  $a$  increases.

Fig. 5 displays the images of the rotating thin accretion disk as viewed at inclination angles  $\theta_o = 17^\circ$  (top row) and  $\theta_o = 89^\circ$  (bottom row), respectively. The disk's rotation induces a pronounced Doppler effect, resulting in a clear left-right asymmetry: emission from matter approaching the observer (left side) is blueshifted and significantly brighter, while emission from receding matter (right side) is redshifted and dimmer. At  $\theta_o = 17^\circ$ , the shadow boundary shows a slight but increasingly noticeable deviation from circularity as  $a$  increases. This deformation manifests as a vertical elongation of the shadow aligned with the magnetic field direction, consistent with the stretching of closed orbits in the meridional plane. The lensing ring maintains a narrow, high-intensity structure that becomes even thinner with increasing  $a$ . At the near-edge-on inclination

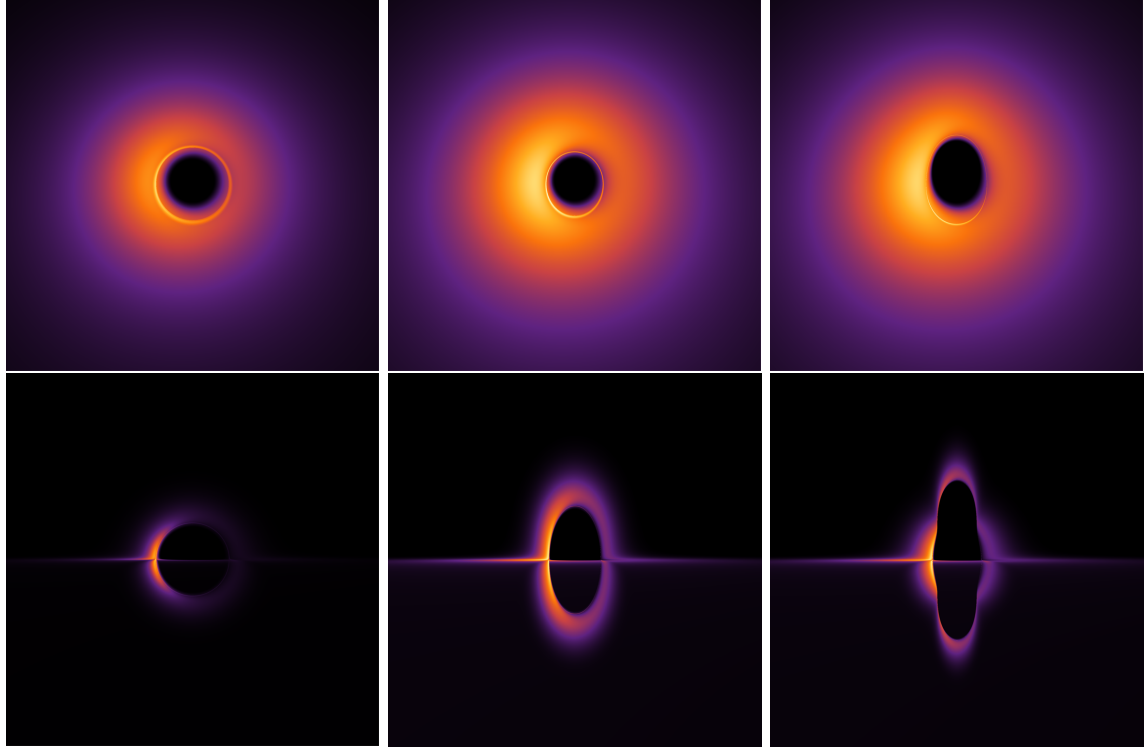


FIG. 5. Images of a rotating accretion disk viewed at inclination angles  $\theta_o = 17^\circ$  (**Top**) and  $\theta_o = 89^\circ$  (**Bottom**), for nonlinearity parameters  $a = 0$  (**Left**),  $0.5$  (**Middle**), and  $2$  (**Right**). For  $\theta_o = 17^\circ$ , the black hole shadow remains nearly circular, though a gradually increasing vertical elongation emerges with increasing  $a$ . The lensing ring remains narrow and bright, and becomes thinner for larger  $a$ . For  $\theta_o = 89^\circ$ , the images appear significantly dimmer due to reduced direct emission, which is confined to a thin horizontal stripe and the upper portion of the bright ring. The lensing ring forms the lower portion of the bright ring. The vertical elongation of the shadow becomes more pronounced at this high inclination.

of  $\theta_o = 89^\circ$ , the total observed flux is significantly reduced. The direct emission consists of a thin horizontal bright stripe across the center and the upper portion of the bright ring surrounding the shadow. In contrast, the lensing ring primarily contributes to the lower portion of the bright ring. As  $a$  increases, the vertical elongation of the shadow becomes more pronounced compared to the lower inclination case.

#### IV. CONCLUSION

In this paper, we first investigated the configuration of an asymptotically uniform BI magnetic field in the fixed background of a Schwarzschild black hole. Our analysis shows that nonlinear electromagnetic effects become significant near the black hole horizon, particularly in the polar regions.

As the nonlinearity parameter  $a$  increases, the magnetic field exhibits a noticeable enhancement near the poles, accompanied by a higher density of field lines in this region. This contrasts with the Maxwell case, where the field remains relatively uniform near the black hole's polar axis.

We also analyzed the motion of light rays in the effective geometry induced by BI magnetic fields. While closed photon orbits remain circular on the equatorial plane, they become prolate on the meridional plane, displaying elongation along the polar axis. This stretching correlates with the amplification of the magnetic field magnitude in the polar regions. Furthermore, we simulated black hole images and shadows in the presence of BI magnetic fields. Our simulations show that the shadow, which is circular in the Maxwell limit, becomes increasingly elongated along the polar direction as  $a$  increases, particularly for large observer inclination angles.

This paper highlights the importance of considering nonlinear electrodynamics in strong gravitational backgrounds, where observable signatures can deviate substantially from predictions based on the Maxwell theory. The distinctive deformations of black hole shadows presented here may serve as potential probes for future high-resolution astronomical observations [96, 98, 99]. Future research will explore these phenomena in the context of rotating black holes, investigate a wider range of the nonlinearity parameters and alternative emission models, and aim to compare theoretical predictions with observational data from facilities like the EHT.

## ACKNOWLEDGMENTS

We are grateful to Lang Cheng and Tianshu Wu for useful discussions and valuable comments. This work is supported in part by NSFC (Grant Nos. 12347133, 12250410250, 12275183 and 12275184) and Discipline Talent Promotion Program of /Xinglin Scholars (Grant No. QNXZ2018050).

- 
- [1] Kazunori Akiyama et al. First M87 Event Horizon Telescope Results. IV. Imaging the Central Supermassive Black Hole. *Astrophys. J. Lett.*, 875(1):L4, 2019. [arXiv:1906.11241](https://arxiv.org/abs/1906.11241), [doi:10.3847/2041-8213/ab0e85](https://doi.org/10.3847/2041-8213/ab0e85). I
  - [2] Kazunori Akiyama et al. First M87 Event Horizon Telescope Results. II. Array and Instrumentation. *Astrophys. J. Lett.*, 875(1):L2, 2019. [arXiv:1906.11239](https://arxiv.org/abs/1906.11239), [doi:10.3847/2041-8213/ab0c96](https://doi.org/10.3847/2041-8213/ab0c96).
  - [3] Kazunori Akiyama et al. First M87 Event Horizon Telescope Results. I. The Shadow of the Supermassive Black Hole. *Astrophys. J. Lett.*, 875:L1, 2019. [arXiv:1906.11238](https://arxiv.org/abs/1906.11238), [doi:10.3847/2041-8213/ab0ec7](https://doi.org/10.3847/2041-8213/ab0ec7).
  - [4] Kazunori Akiyama et al. First M87 Event Horizon Telescope Results. VI. The Shadow and Mass

- of the Central Black Hole. *Astrophys. J. Lett.*, 875(1):L6, 2019. [arXiv:1906.11243](https://arxiv.org/abs/1906.11243), [doi:10.3847/2041-8213/ab1141](https://doi.org/10.3847/2041-8213/ab1141).
- [5] Kazunori Akiyama et al. First M87 Event Horizon Telescope Results. V. Physical Origin of the Asymmetric Ring. *Astrophys. J. Lett.*, 875(1):L5, 2019. [arXiv:1906.11242](https://arxiv.org/abs/1906.11242), [doi:10.3847/2041-8213/ab0f43](https://doi.org/10.3847/2041-8213/ab0f43).
- [6] Kazunori Akiyama et al. First M87 Event Horizon Telescope Results. III. Data Processing and Calibration. *Astrophys. J. Lett.*, 875(1):L3, 2019. [arXiv:1906.11240](https://arxiv.org/abs/1906.11240), [doi:10.3847/2041-8213/ab0c57](https://doi.org/10.3847/2041-8213/ab0c57). I
- [7] Kazunori Akiyama et al. First Sagittarius A\* Event Horizon Telescope Results. I. The Shadow of the Supermassive Black Hole in the Center of the Milky Way. *Astrophys. J. Lett.*, 930(2):L12, 2022. [doi:10.3847/2041-8213/ac6674](https://doi.org/10.3847/2041-8213/ac6674). I
- [8] Kazunori Akiyama et al. First Sagittarius A\* Event Horizon Telescope Results. II. EHT and Multiwavelength Observations, Data Processing, and Calibration. *Astrophys. J. Lett.*, 930(2):L13, 2022. [doi:10.3847/2041-8213/ac6675](https://doi.org/10.3847/2041-8213/ac6675).
- [9] Kazunori Akiyama et al. First Sagittarius A\* Event Horizon Telescope Results. III. Imaging of the Galactic Center Supermassive Black Hole. *Astrophys. J. Lett.*, 930(2):L14, 2022. [doi:10.3847/2041-8213/ac6429](https://doi.org/10.3847/2041-8213/ac6429).
- [10] Kazunori Akiyama et al. First Sagittarius A\* Event Horizon Telescope Results. IV. Variability, Morphology, and Black Hole Mass. *Astrophys. J. Lett.*, 930(2):L15, 2022. [doi:10.3847/2041-8213/ac6736](https://doi.org/10.3847/2041-8213/ac6736).
- [11] Kazunori Akiyama et al. First Sagittarius A\* Event Horizon Telescope Results. V. Testing Astrophysical Models of the Galactic Center Black Hole. *Astrophys. J. Lett.*, 930(2):L16, 2022. [doi:10.3847/2041-8213/ac6672](https://doi.org/10.3847/2041-8213/ac6672).
- [12] Kazunori Akiyama et al. First Sagittarius A\* Event Horizon Telescope Results. VI. Testing the Black Hole Metric. *Astrophys. J. Lett.*, 930(2):L17, 2022. [doi:10.3847/2041-8213/ac6756](https://doi.org/10.3847/2041-8213/ac6756). I
- [13] J. L. Synge. The Escape of Photons from Gravitationally Intense Stars. *Mon. Not. Roy. Astron. Soc.*, 131(3):463–466, 1966. [doi:10.1093/mnras/131.3.463](https://doi.org/10.1093/mnras/131.3.463). I
- [14] James M. Bardeen, William H. Press, and Saul A Teukolsky. Rotating black holes: Locally nonrotating frames, energy extraction, and scalar synchrotron radiation. *Astrophys. J.*, 178:347, 1972. [doi:10.1086/151796](https://doi.org/10.1086/151796).
- [15] J. M. Bardeen. Timelike and null geodesics in the Kerr metric. In *Les Houches Summer School of Theoretical Physics: Black Holes*, 1973.
- [16] Valerio Bozza. Gravitational Lensing by Black Holes. *Gen. Rel. Grav.*, 42:2269–2300, 2010. [arXiv:0911.2187](https://arxiv.org/abs/0911.2187), [doi:10.1007/s10714-010-0988-2](https://doi.org/10.1007/s10714-010-0988-2). I
- [17] Zilong Li and Cosimo Bambi. Measuring the Kerr spin parameter of regular black holes from their shadow. *JCAP*, 01:041, 2014. [arXiv:1309.1606](https://arxiv.org/abs/1309.1606), [doi:10.1088/1475-7516/2014/01/041](https://doi.org/10.1088/1475-7516/2014/01/041). I
- [18] Naoki Tsukamoto, Zilong Li, and Cosimo Bambi. Constraining the spin and the deformation parameters

- from the black hole shadow. *JCAP*, 06:043, 2014. [arXiv:1403.0371](https://arxiv.org/abs/1403.0371), doi:10.1088/1475-7516/2014/06/043.
- [19] Rahul Kumar and Sushant G. Ghosh. Black Hole Parameter Estimation from Its Shadow. *Astrophys. J.*, 892:78, 2020. [arXiv:1811.01260](https://arxiv.org/abs/1811.01260), doi:10.3847/1538-4357/ab77b0.
  - [20] Cosimo Bambi, Katherine Freese, Sunny Vagnozzi, and Luca Visinelli. Testing the rotational nature of the supermassive object M87\* from the circularity and size of its first image. *Phys. Rev. D*, 100(4):044057, 2019. [arXiv:1904.12983](https://arxiv.org/abs/1904.12983), doi:10.1103/PhysRevD.100.044057.
  - [21] Misba Afrin, Sunny Vagnozzi, and Sushant G. Ghosh. Tests of Loop Quantum Gravity from the Event Horizon Telescope Results of Sgr A\*. *Astrophys. J.*, 944(2):149, 2023. [arXiv:2209.12584](https://arxiv.org/abs/2209.12584), doi:10.3847/1538-4357/acb334.
  - [22] Zi-Liang Wang and Emmanuele Battista. Dynamical features and shadows of quantum Schwarzschild black hole in effective field theories of gravity. *Eur. Phys. J. C*, 85(3):304, 2025. [arXiv:2501.14516](https://arxiv.org/abs/2501.14516), doi:10.1140/epjc/s10052-025-13833-7. I
  - [23] Pedro V. P. Cunha, Carlos A. R. Herdeiro, Eugen Radu, and Helgi F. Runarsson. Shadows of Kerr black holes with scalar hair. *Phys. Rev. Lett.*, 115(21):211102, 2015. [arXiv:1509.00021](https://arxiv.org/abs/1509.00021), doi:10.1103/PhysRevLett.115.211102. I
  - [24] Pedro V. P. Cunha, Carlos A. R. Herdeiro, Eugen Radu, and Helgi F. Runarsson. Shadows of Kerr black holes with and without scalar hair. *Int. J. Mod. Phys. D*, 25(09):1641021, 2016. [arXiv:1605.08293](https://arxiv.org/abs/1605.08293), doi:10.1142/S0218271816410212.
  - [25] Mohsen Khodadi, Alireza Allahyari, Sunny Vagnozzi, and David F. Mota. Black holes with scalar hair in light of the Event Horizon Telescope. *JCAP*, 09:026, 2020. [arXiv:2005.05992](https://arxiv.org/abs/2005.05992), doi:10.1088/1475-7516/2020/09/026.
  - [26] Qingyu Gan, Peng Wang, Houwen Wu, and Haitang Yang. Photon spheres and spherical accretion image of a hairy black hole. *Phys. Rev. D*, 104(2):024003, 2021. [arXiv:2104.08703](https://arxiv.org/abs/2104.08703), doi:10.1103/PhysRevD.104.024003.
  - [27] Qingyu Gan, Peng Wang, Houwen Wu, and Haitang Yang. Photon ring and observational appearance of a hairy black hole. *Phys. Rev. D*, 104(4):044049, 2021. [arXiv:2105.11770](https://arxiv.org/abs/2105.11770), doi:10.1103/PhysRevD.104.044049.
  - [28] Rajes Ghosh, Selim Sk, and Sudipta Sarkar. Hairy Black Holes: Non-existence of Short Hairs and Bound on Light Ring Size. 6 2023. [arXiv:2306.14193](https://arxiv.org/abs/2306.14193).
  - [29] Pedro G. S. Fernandes, Clare Burrage, Astrid Eichhorn, and Thomas P. Sotiriou. Shadows and properties of spin-induced scalarized black holes with and without a Ricci coupling. *Phys. Rev. D*, 109(10):104033, 2024. [arXiv:2403.14596](https://arxiv.org/abs/2403.14596), doi:10.1103/PhysRevD.109.104033.
  - [30] Xi-Jing Wang, Yuan Meng, Xiao-Mei Kuang, and Kai Liao. Distinguishing black holes with and without spontaneous scalarization in Einstein-scalar-Gauss-Bonnet theories via optical features. *Eur. Phys. J. C*, 84(12):1243, 2024. [arXiv:2409.20200](https://arxiv.org/abs/2409.20200), doi:10.1140/epjc/s10052-024-13612-w. I
  - [31] Leonardo Amarilla and Ernesto F. Eiroa. Shadow of a rotating braneworld black hole. *Phys. Rev. D*,

- 85:064019, 2012. [arXiv:1112.6349](https://arxiv.org/abs/1112.6349), doi:[10.1103/PhysRevD.85.064019](https://doi.org/10.1103/PhysRevD.85.064019). I
- [32] Minyong Guo, Shupeng Song, and Haopeng Yan. Observational signature of a near-extremal Kerr-Sen black hole in the heterotic string theory. *Phys. Rev. D*, 101(2):024055, 2020. [arXiv:1911.04796](https://arxiv.org/abs/1911.04796), doi:[10.1103/PhysRevD.101.024055](https://doi.org/10.1103/PhysRevD.101.024055).
- [33] Tao Zhu, Qiang Wu, Mubasher Jamil, and Kimet Jusufi. Shadows and deflection angle of charged and slowly rotating black holes in Einstein- $\mathcal{E}$ ther theory. *Phys. Rev. D*, 100(4):044055, 2019. [arXiv:1906.05673](https://arxiv.org/abs/1906.05673), doi:[10.1103/PhysRevD.100.044055](https://doi.org/10.1103/PhysRevD.100.044055).
- [34] Rahul Kumar, Sushant G. Ghosh, and Anzhong Wang. Gravitational deflection of light and shadow cast by rotating Kalb-Ramond black holes. *Phys. Rev. D*, 101(10):104001, 2020. [arXiv:2001.00460](https://arxiv.org/abs/2001.00460), doi:[10.1103/PhysRevD.101.104001](https://doi.org/10.1103/PhysRevD.101.104001). I
- [35] Fabio Bacchini, Daniel R. Mayerson, Bart Ripperda, Jordy Davelaar, Héctor Olivares, Thomas Hertog, and Bert Vercnocke. Fuzzball Shadows: Emergent Horizons from Microstructure. *Phys. Rev. Lett.*, 127(17):171601, 2021. [arXiv:2103.12075](https://arxiv.org/abs/2103.12075), doi:[10.1103/PhysRevLett.127.171601](https://doi.org/10.1103/PhysRevLett.127.171601). I
- [36] Pedro V. P. Cunha, José A. Font, Carlos Herdeiro, Eugen Radu, Nicolas Sanchis-Gual, and Miguel Zilhão. Lensing and dynamics of ultracompact bosonic stars. *Phys. Rev. D*, 96(10):104040, 2017. [arXiv:1709.06118](https://arxiv.org/abs/1709.06118), doi:[10.1103/PhysRevD.96.104040](https://doi.org/10.1103/PhysRevD.96.104040). I
- [37] Pedro V. P. Cunha and Carlos A. R. Herdeiro. Shadows and strong gravitational lensing: a brief review. *Gen. Rel. Grav.*, 50(4):42, 2018. [arXiv:1801.00860](https://arxiv.org/abs/1801.00860), doi:[10.1007/s10714-018-2361-9](https://doi.org/10.1007/s10714-018-2361-9). III A
- [38] Rajibul Shaikh, Pritam Banerjee, Suvankar Paul, and Tapobrata Sarkar. A novel gravitational lensing feature by wormholes. *Phys. Lett. B*, 789:270–275, 2019. [Erratum: Phys.Lett.B 791, 422–423 (2019)]. [arXiv:1811.08245](https://arxiv.org/abs/1811.08245), doi:[10.1016/j.physletb.2018.12.030](https://doi.org/10.1016/j.physletb.2018.12.030).
- [39] Rajibul Shaikh, Pritam Banerjee, Suvankar Paul, and Tapobrata Sarkar. Analytical approach to strong gravitational lensing from ultracompact objects. *Phys. Rev. D*, 99(10):104040, 2019. [arXiv:1903.08211](https://arxiv.org/abs/1903.08211), doi:[10.1103/PhysRevD.99.104040](https://doi.org/10.1103/PhysRevD.99.104040).
- [40] Rajibul Shaikh, Pritam Banerjee, Suvankar Paul, and Tapobrata Sarkar. Strong gravitational lensing by wormholes. *JCAP*, 07:028, 2019. [arXiv:1905.06932](https://arxiv.org/abs/1905.06932), doi:[10.1088/1475-7516/2019/07/028](https://doi.org/10.1088/1475-7516/2019/07/028).
- [41] Maciek Wielgus, Jiri Horak, Frederic Vincent, and Marek Abramowicz. Reflection-asymmetric wormholes and their double shadows. *Phys. Rev. D*, 102(8):084044, 2020. [arXiv:2008.10130](https://arxiv.org/abs/2008.10130), doi:[10.1103/PhysRevD.102.084044](https://doi.org/10.1103/PhysRevD.102.084044).
- [42] Jun Peng, Minyong Guo, and Xing-Hui Feng. Observational signature and additional photon rings of an asymmetric thin-shell wormhole. *Phys. Rev. D*, 104(12):124010, 2021. [arXiv:2102.05488](https://arxiv.org/abs/2102.05488), doi:[10.1103/PhysRevD.104.124010](https://doi.org/10.1103/PhysRevD.104.124010).
- [43] Hyat Huang, Jutta Kunz, and Deeshani Mitra. Shadow images of compact objects in beyond Horndeski theory. *JCAP*, 05:007, 2024. [arXiv:2401.15249](https://arxiv.org/abs/2401.15249), doi:[10.1088/1475-7516/2024/05/007](https://doi.org/10.1088/1475-7516/2024/05/007). I
- [44] Ashok B. Joshi, Dipanjan Dey, Pankaj S. Joshi, and Parth Bambhaniya. Shadow of a Naked Singularity without Photon Sphere. *Phys. Rev. D*, 102(2):024022, 2020. [arXiv:2004.06525](https://arxiv.org/abs/2004.06525), doi:[10.1103/PhysRevD.102.024022](https://doi.org/10.1103/PhysRevD.102.024022). I

- [45] Dipanjan Dey, Rajibul Shaikh, and Pankaj S. Joshi. Shadow of nulllike and timelike naked singularities without photon spheres. *Phys. Rev. D*, 103(2):024015, 2021. [arXiv:2009.07487](https://arxiv.org/abs/2009.07487), doi:10.1103/PhysRevD.103.024015.
- [46] Yiqian Chen, Peng Wang, Houwen Wu, and Haitang Yang. Gravitational lensing by Born-Infeld naked singularities. *Phys. Rev. D*, 109(8):084014, 2024. [arXiv:2305.17411](https://arxiv.org/abs/2305.17411), doi:10.1103/PhysRevD.109.084014.
- [47] Yiqian Chen, Peng Wang, Houwen Wu, and Haitang Yang. Observations of orbiting hot spots around naked singularities. *JCAP*, 04:032, 2024. [arXiv:2309.04157](https://arxiv.org/abs/2309.04157), doi:10.1088/1475-7516/2024/04/032.
- [48] Valentin Deliyski, Galin Gyulchev, Petya Nedkova, and Stoytcho Yazadjiev. Observing naked singularities with the present and next-generation Event Horizon Telescope. *Phys. Rev. D*, 111(6):064068, 2025. [arXiv:2401.14092](https://arxiv.org/abs/2401.14092), doi:10.1103/PhysRevD.111.064068. I
- [49] Leonardo Amarilla, Ernesto F. Eiroa, and Gaston Giribet. Null geodesics and shadow of a rotating black hole in extended Chern-Simons modified gravity. *Phys. Rev. D*, 81:124045, 2010. [arXiv:1005.0607](https://arxiv.org/abs/1005.0607), doi:10.1103/PhysRevD.81.124045. I
- [50] Dimitry Ayzenberg and Nicolas Yunes. Black Hole Shadow as a Test of General Relativity: Quadratic Gravity. *Class. Quant. Grav.*, 35(23):235002, 2018. [arXiv:1807.08422](https://arxiv.org/abs/1807.08422), doi:10.1088/1361-6382/aae87b.
- [51] Hui-Min Wang, Yu-Meng Xu, and Shao-Wen Wei. Shadows of Kerr-like black holes in a modified gravity theory. *JCAP*, 03:046, 2019. [arXiv:1810.12767](https://arxiv.org/abs/1810.12767), doi:10.1088/1475-7516/2019/03/046.
- [52] Liang Ma and H. Lu. Bounds on photon spheres and shadows of charged black holes in Einstein-Gauss-Bonnet-Maxwell gravity. *Phys. Lett. B*, 807:135535, 2020. [arXiv:1912.05569](https://arxiv.org/abs/1912.05569), doi:10.1016/j.physletb.2020.135535.
- [53] Minyong Guo and Peng-Cheng Li. Innermost stable circular orbit and shadow of the 4D Einstein-Gauss-Bonnet black hole. *Eur. Phys. J. C*, 80(6):588, 2020. [arXiv:2003.02523](https://arxiv.org/abs/2003.02523), doi:10.1140/epjc/s10052-020-8164-7.
- [54] Shao-Wen Wei and Yu-Xiao Liu. Testing the nature of Gauss-Bonnet gravity by four-dimensional rotating black hole shadow. *Eur. Phys. J. Plus*, 136(4):436, 2021. [arXiv:2003.07769](https://arxiv.org/abs/2003.07769), doi:10.1140/epjp/s13360-021-01398-9.
- [55] Xiao-Xiong Zeng, Hai-Qing Zhang, and Hongbao Zhang. Shadows and photon spheres with spherical accretions in the four-dimensional Gauss-Bonnet black hole. *Eur. Phys. J. C*, 80(9):872, 2020. [arXiv:2004.12074](https://arxiv.org/abs/2004.12074), doi:10.1140/epjc/s10052-020-08449-y.
- [56] Andrea Addazi, Salvatore Capozziello, and Sergei Odintsov. Chaotic solutions and black hole shadow in  $f(R)$  gravity. *Phys. Lett. B*, 816:136257, 2021. [arXiv:2103.16856](https://arxiv.org/abs/2103.16856), doi:10.1016/j.physletb.2021.136257.
- [57] Hui-Min Wang, Zi-Chao Lin, and Shao-Wen Wei. Optical appearance of Einstein-Æther black hole surrounded by thin disk. *Nucl. Phys. B*, 985:116026, 2022. [arXiv:2205.13174](https://arxiv.org/abs/2205.13174), doi:10.1016/j.nuclphysb.2022.116026.

- [58] Wentao Liu, Di Wu, and Jieci Wang. Shadow of slowly rotating Kalb-Ramond black holes. *JCAP*, 05:017, 2025. [arXiv:2407.07416](https://arxiv.org/abs/2407.07416), doi:10.1088/1475-7516/2025/05/017. I
- [59] Kazunori Akiyama et al. First M87 Event Horizon Telescope Results. VII. Polarization of the Ring. *Astrophys. J. Lett.*, 910(1):L12, 2021. [arXiv:2105.01169](https://arxiv.org/abs/2105.01169), doi:10.3847/2041-8213/abe71d. I
- [60] Igor V. Igumenshchev, Ramesh Narayan, and Marek A. Abramowicz. Three-dimensional mhd simulations of radiatively inefficient accretion flows. *Astrophys. J.*, 592:1042–1059, 2003. [arXiv:astro-ph/0301402](https://arxiv.org/abs/astro-ph/0301402), doi:10.1086/375769. I
- [61] Ramesh Narayan, Igor V. Igumenshchev, and Marek A. Abramowicz. Magnetically arrested disk: an energetically efficient accretion flow. *Publ. Astron. Soc. Jap.*, 55:L69, 2003. [arXiv:astro-ph/0305029](https://arxiv.org/abs/astro-ph/0305029), doi:10.1093/pasj/55.6.L69.
- [62] Kazunori Akiyama et al. First M87 Event Horizon Telescope Results. VIII. Magnetic Field Structure near The Event Horizon. *Astrophys. J. Lett.*, 910(1):L13, 2021. [arXiv:2105.01173](https://arxiv.org/abs/2105.01173), doi:10.3847/2041-8213/abe4de. I
- [63] R. P. Eatough et al. A strong magnetic field around the supermassive black hole at the centre of the Galaxy. *Nature*, 501:391–394, 2013. [arXiv:1308.3147](https://arxiv.org/abs/1308.3147), doi:10.1038/nature12499. I
- [64] Haroldo C. D. Lima Junior, Jian-Zhi Yang, Luís C. B. Crispino, Pedro V. P. Cunha, and Carlos A. R. Herdeiro. Einstein-Maxwell-dilaton neutral black holes in strong magnetic fields: Topological charge, shadows, and lensing. *Phys. Rev. D*, 105(6):064070, 2022. [arXiv:2112.10802](https://arxiv.org/abs/2112.10802), doi:10.1103/PhysRevD.105.064070. I
- [65] Mingzhi Wang, Songbai Chen, and Jiliang Jing. Kerr black hole shadows in Melvin magnetic field with stable photon orbits. *Phys. Rev. D*, 104(8):084021, 2021. [arXiv:2104.12304](https://arxiv.org/abs/2104.12304), doi:10.1103/PhysRevD.104.084021.
- [66] Yehui Hou, Zhenyu Zhang, Haopeng Yan, Minyong Guo, and Bin Chen. Image of a Kerr-Melvin black hole with a thin accretion disk. *Phys. Rev. D*, 106(6):064058, 2022. [arXiv:2206.13744](https://arxiv.org/abs/2206.13744), doi:10.1103/PhysRevD.106.064058. I
- [67] Farruh Atamurotov, Sushant G. Ghosh, and Bobomurat Ahmedov. Horizon structure of rotating Einstein–Born–Infeld black holes and shadow. *Eur. Phys. J. C*, 76(5):273, 2016. [arXiv:1506.03690](https://arxiv.org/abs/1506.03690), doi:10.1140/epjc/s10052-016-4122-9. I
- [68] Zdenek Stuchlík and Jan Schee. Shadow of the regular Bardeen black holes and comparison of the motion of photons and neutrinos. *Eur. Phys. J. C*, 79(1):44, 2019. doi:10.1140/epjc/s10052-019-6543-8.
- [69] Alireza Allahyari, Mohsen Khodadi, Sunny Vagnozzi, and David F. Mota. Magnetically charged black holes from non-linear electrodynamics and the Event Horizon Telescope. *JCAP*, 02:003, 2020. [arXiv:1912.08231](https://arxiv.org/abs/1912.08231), doi:10.1088/1475-7516/2020/02/003.
- [70] Soroush Zare, Luis M. Nieto, Xing-Hui Feng, Shi-Hai Dong, and Hassan Hassanabadi. Shadows, rings and optical appearance of a magnetically charged regular black hole illuminated by various accretion disks. *JCAP*, 08:041, 2024. [arXiv:2406.07300](https://arxiv.org/abs/2406.07300), doi:10.1088/1475-7516/2024/08/041.

- [71] A. A. Araújo Filho. Analysis of a nonlinear electromagnetic generalization of the Reissner–Nordström black hole. *Eur. Phys. J. C*, 85(4):454, 2025. [arXiv:2410.12060](https://arxiv.org/abs/2410.12060), doi:[10.1140/epjc/s10052-025-14182-1](https://doi.org/10.1140/epjc/s10052-025-14182-1). I
- [72] Zezhou Hu, Zhen Zhong, Peng-Cheng Li, Minyong Guo, and Bin Chen. QED effect on a black hole shadow. *Phys. Rev. D*, 103(4):044057, 2021. [arXiv:2012.07022](https://arxiv.org/abs/2012.07022), doi:[10.1103/PhysRevD.103.044057](https://doi.org/10.1103/PhysRevD.103.044057). I
- [73] Zhen Zhong, Zezhou Hu, Haopeng Yan, Minyong Guo, and Bin Chen. QED effects on Kerr black hole shadows immersed in uniform magnetic fields. *Phys. Rev. D*, 104(10):104028, 2021. [arXiv:2108.06140](https://arxiv.org/abs/2108.06140), doi:[10.1103/PhysRevD.104.104028](https://doi.org/10.1103/PhysRevD.104.104028).
- [74] Aoyun He, Jun Tao, Peng Wang, Yadong Xue, and Lingkai Zhang. Effects of Born–Infeld electrodynamics on black hole shadows. *Eur. Phys. J. C*, 82(8):683, 2022. [arXiv:2205.12779](https://arxiv.org/abs/2205.12779), doi:[10.1140/epjc/s10052-022-10637-x](https://doi.org/10.1140/epjc/s10052-022-10637-x). I, II, III A, 1
- [75] E. S. Fradkin and Arkady A. Tseytlin. Nonlinear Electrodynamics from Quantized Strings. *Phys. Lett. B*, 163:123–130, 1985. doi:[10.1016/0370-2693\(85\)90205-9](https://doi.org/10.1016/0370-2693(85)90205-9). I
- [76] Arkady A. Tseytlin. Vector Field Effective Action in the Open Superstring Theory. *Nucl. Phys. B*, 276:391, 1986. [Erratum: Nucl.Phys.B 291, 876 (1987)]. doi:[10.1016/0550-3213\(86\)90303-2](https://doi.org/10.1016/0550-3213(86)90303-2).
- [77] I. H. Salazar, A. Garcia, and J. Plebanski. Duality Rotations and Type D Solutions to Einstein Equations With Nonlinear Electromagnetic Sources. *J. Math. Phys.*, 28:2171–2181, 1987. doi:[10.1063/1.527430](https://doi.org/10.1063/1.527430).
- [78] David L. Wiltshire. Black Holes in String Generated Gravity Models. *Phys. Rev. D*, 38:2445, 1988. doi:[10.1103/PhysRevD.38.2445](https://doi.org/10.1103/PhysRevD.38.2445). I
- [79] M. Born and L. Infeld. Foundations of the new field theory. *Proc. Roy. Soc. Lond. A*, 144(852):425–451, 1934. doi:[10.1098/rspa.1934.0059](https://doi.org/10.1098/rspa.1934.0059). I, II
- [80] Rong-Gen Cai, Da-Wei Pang, and Anzhong Wang. Born-Infeld black holes in (A)dS spaces. *Phys. Rev. D*, 70:124034, 2004. [arXiv:hep-th/0410158](https://arxiv.org/abs/hep-th/0410158), doi:[10.1103/PhysRevD.70.124034](https://doi.org/10.1103/PhysRevD.70.124034). I
- [81] Tanay Kr. Dey. Born-Infeld black holes in the presence of a cosmological constant. *Phys. Lett. B*, 595(1-4):484–490, 2004. [arXiv:hep-th/0406169](https://arxiv.org/abs/hep-th/0406169), doi:[10.1016/j.physletb.2004.06.047](https://doi.org/10.1016/j.physletb.2004.06.047).
- [82] Sharmanthie Fernando. Thermodynamics of Born-Infeld-anti-de Sitter black holes in the grand canonical ensemble. *Phys. Rev. D*, 74:104032, 2006. [arXiv:hep-th/0608040](https://arxiv.org/abs/hep-th/0608040), doi:[10.1103/PhysRevD.74.104032](https://doi.org/10.1103/PhysRevD.74.104032).
- [83] Olivera Miskovic and Rodrigo Olea. Thermodynamics of Einstein-Born-Infeld black holes with negative cosmological constant. *Phys. Rev. D*, 77:124048, 2008. [arXiv:0802.2081](https://arxiv.org/abs/0802.2081), doi:[10.1103/PhysRevD.77.124048](https://doi.org/10.1103/PhysRevD.77.124048).
- [84] Sharmila Gunasekaran, Robert B. Mann, and David Kubiznak. Extended phase space thermodynamics for charged and rotating black holes and Born-Infeld vacuum polarization. *JHEP*, 11:110, 2012. [arXiv:1208.6251](https://arxiv.org/abs/1208.6251), doi:[10.1007/JHEP11\(2012\)110](https://doi.org/10.1007/JHEP11(2012)110).
- [85] De-Cheng Zou, Shao-Jun Zhang, and Bin Wang. Critical behavior of Born-Infeld AdS black holes in

- the extended phase space thermodynamics. *Phys. Rev. D*, 89(4):044002, Feb 2014. URL: <https://link.aps.org/doi/10.1103/PhysRevD.89.044002>, arXiv:1311.7299, doi:10.1103/PhysRevD.89.044002.
- [86] Jun Tao, Peng Wang, and Haitang Yang. Testing holographic conjectures of complexity with Born–Infeld black holes. *Eur. Phys. J. C*, 77(12):817, 2017. arXiv:1703.06297, doi:10.1140/epjc/s10052-017-5395-3.
- [87] Peng Wang, Houwen Wu, and Haitang Yang. Thermodynamics and Phase Transitions of Nonlinear Electrodynamics Black Holes in an Extended Phase Space. *JCAP*, 04(04):052, 2019. arXiv:1808.04506, doi:10.1088/1475-7516/2019/04/052.
- [88] Qingyu Gan, Guangzhou Guo, Peng Wang, and Houwen Wu. Strong cosmic censorship for a scalar field in a Born-Infeld–de Sitter black hole. *Phys. Rev. D*, 100(12):124009, 2019. arXiv:1907.04466, doi:10.1103/PhysRevD.100.124009.
- [89] Peng Wang, Houwen Wu, and Haitang Yang. Thermodynamics and Phase Transition of a Nonlinear Electrodynamics Black Hole in a Cavity. *JHEP*, 07:002, 2019. arXiv:1901.06216, doi:10.1007/JHEP07(2019)002.
- [90] Peng Wang, Houwen Wu, and Haitang Yang. Scalarized Einstein-Born-Infeld black holes. *Phys. Rev. D*, 103(10):104012, 2021. arXiv:2012.01066, doi:10.1103/PhysRevD.103.104012. I
- [91] Ana Bokulić and Ivica Smolić. Schwarzschild spacetime immersed in test nonlinear electromagnetic fields. *Class. Quant. Grav.*, 37(5):055004, 2020. arXiv:1910.04219, doi:10.1088/1361-6382/ab6390. I, II, III
- [92] Robert M. Wald. Black hole in a uniform magnetic field. *Phys. Rev. D*, 10:1680–1685, 1974. doi:10.1103/PhysRevD.10.1680. II
- [93] John P Boyd. *Chebyshev and Fourier spectral methods*. Courier Corporation, 2001. II
- [94] M. Novello, V. A. De Lorenci, J. M. Salim, and Renato Klippert. Geometrical aspects of light propagation in nonlinear electrodynamics. *Phys. Rev. D*, 61:045001, 2000. arXiv:gr-qc/9911085, doi:10.1103/PhysRevD.61.045001. III A
- [95] Guangzhou Guo, Xin Jiang, Peng Wang, and Houwen Wu. Gravitational lensing by black holes with multiple photon spheres. *Phys. Rev. D*, 105(12):124064, 2022. arXiv:2204.13948, doi:10.1103/PhysRevD.105.124064. III B
- [96] Samuel E. Gralla, Alexandru Lupsasca, and Daniel P. Marrone. The shape of the black hole photon ring: A precise test of strong-field general relativity. *Phys. Rev. D*, 102(12):124004, 2020. arXiv:2008.03879, doi:10.1103/PhysRevD.102.124004. III C, III C, IV
- [97] Samuel E. Gralla, Daniel E. Holz, and Robert M. Wald. Black Hole Shadows, Photon Rings, and Lensing Rings. *Phys. Rev. D*, 100(2):024018, 2019. arXiv:1906.00873, doi:10.1103/PhysRevD.100.024018. III C
- [98] Michael D. Johnson et al. Universal interferometric signatures of a black hole’s photon ring. *Sci. Adv.*, 6(12):eaaz1310, 2020. arXiv:1907.04329, doi:10.1126/sciadv.aaz1310. IV

- [99] Elizabeth Himwich, Michael D. Johnson, Alexandru Lupsasca, and Andrew Strominger. Universal polarimetric signatures of the black hole photon ring. *Phys. Rev. D*, 101(8):084020, 2020. [arXiv:2001.08750](https://arxiv.org/abs/2001.08750), [doi:10.1103/PhysRevD.101.084020](https://doi.org/10.1103/PhysRevD.101.084020). IV